Research Article

Synergetic effect of lattice distortion and oxygen vacancies on high-rate lithium-ion storage in high-entropy perovskite oxides

Yanggang Jia[a], Shijie Chen[a], Xia Shao[a], Jie Chen[a], Dao-Lai Fang[a],
Saisai Li[a], Aiqin Mao[a,b,*], Canhua Li[c,*]

[a]*School of Materials Science and Engineering, Anhui University of Technology,
Ma'anshan 243032, China*
[b]*Key Laboratory of Green Fabrication and Surface Technology of Advanced Metal Materials,
Ministry of Education, Anhui University of Technology, Ma'anshan 243002, China*
[c]*School of Metallurgical Engineering, Anhui University of Technology, Ma'anshan 243032, China*

Abstract: High-entropy oxides (HEOs) have gained great attention as an emerging kind of high-performance anode materials for lithium-ion batteries (LIBs) due to the entropy stabilization and multi-principal synergistic effect. Herein, the porous perovskite-type $RE(Co_{0.2}Cr_{0.2}Fe_{0.2}Mn_{0.2}Ni_{0.2})O_3$ (RE (= La, Sm, and Gd) is the abbreviation of rare earth) HEOs were successfully synthesized by a solution combustion synthesis (SCS) method. Owing to the synergistic effect of lattice distortion and oxygen vacancies (O_V), the $Gd(Co_{0.2}Cr_{0.2}Fe_{0.2}Mn_{0.2}Ni_{0.2})O_3$ electrode exhibits superior high-rate lithium-ion storage performance and excellent cycling stability. A reversible capacity of 403 $mAh \cdot g^{-1}$ at a current rate of 0.2 $A \cdot g^{-1}$ after 500 cycles and a superior high-rate capacity of 394 $mAh \cdot g^{-1}$ even at 1.0 $A \cdot g^{-1}$ after 500 cycles are achieved. Meanwhile, the $Gd(Co_{0.2}Cr_{0.2}Fe_{0.2}Mn_{0.2}Ni_{0.2})O_3$ electrode also exhibits a pronounced pseudo-capacitive behavior, contributing to an additional capacity. By adjusting and balancing the lattice distortion and oxygen vacancies of the electrode materials, the lithium-ion storage performance can be further regulated.

Keywords: high-entropy anode; perovskite oxides; lattice distortion; oxygen vacancies (O_V); pseudocapacitance; high-rate performance

1 Introduction

Recently, transition metal (TM)-based high-entropy oxides (HEOs) with the incorporation of multi-principal metal cations into a single-phase solid solution structure, have drawn considerable attention as a new class of high-performance electrode active materials for energy storage application [1–8]. These materials show significantly superior structural stability and improved solubility limits, with most of the exceptional performance coming from synergistic effect, beyond a simple rule of mixing. In 2016, Bérardan *et al.* [9] firstly reported that Li- and Na-substituted rock-salt $(Co_{0.2}Cu_{0.2}Mg_{0.2}Ni_{0.2}Zn_{0.2})O$ HEOs exhibited superionic conductivity (Li$^+$: > 10^{-3} S·cm^{-1}; Na$^+$: 5×10^{-6} S·cm^{-1}) at room temperature,

---

* Corresponding authors.
E-mail: A. Mao, maoaiqin@ahut.edu.cn;
      C. Li, Licanhua@ahut.edu.cn

which makes them have potential applications for energy storage. Subsequently, for the first time, $(Co_{0.2}Cu_{0.2}Mg_{0.2}Ni_{0.2}Zn_{0.2})O$ HEO was used as an anode material for lithium-ion batteries (LIBs) by Sarkar *et al*. [1], and demonstrated excellent reversibility and cycling stability owing to the special entropy stabilization and attractive multi-principal synergetic effect. Thereafter, tremendous efforts have been done not only on this rock-salt-type HEO [10–12], but also on spinel-type HEOs as the anode materials for next-generation LIBs owing to their excellent cycling stability [4,13–19], which is attributed, at least to some degree, to the entropy-stabilized structure.

Perovskite oxides with a general formula of ABO_3 are considered as an attractive class of energy storage materials, especially in the field of LIB application due to their stable structure, easily cation substitution at A-site, B-site, or AB-sites, rich oxygen vacancy (O_V), and variable oxidation states [20–22]. To address the aforementioned advantages of HEOs, perovskite-type HEOs have been reported as LIB anode materials. Yan *et al*. [23] first synthesized a novel perovskite-type $[(Bi,Na)_{1/5}(La,Li)_{1/5}(Ce,K)_{1/5}Ca_{1/5}Sr_{1/5}]TiO_3$ HEO and served as a conversion-type anode for LIBs. Different from conventional ABO_3, benefiting from the entropy-stabilized structure and the charge compensation mechanism in HEO, the as-synthesized LIBs exhibited an outstanding lithium-ion storage capacity of 120.4 mAh·g^{-1} at a current rate of 1 A·g^{-1} with a capacity retention of 100% after 300 cycles and a superior rate capacity of 70 mAh·g^{-1} at 3 A·g^{-1}. To further improve the energy storage performance, several promising strategies have been explored and adopted recently. Among them, one effective strategy is atomic engineering to regulate the HEO lattice distortion to offer abundant ion transport pathways [18]. Furthermore, vacancy engineering can notably increase the intrinsic electric conductivity, along with additional active sites for fast redox reactions [4]. In addition, morphological engineering of mesoporous HEOs can facilitate the ion transport without the degradation of electronic transport rate [24].
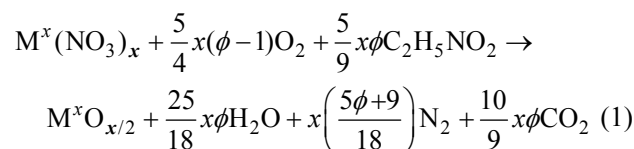
Taking the above-mentioned factors into consideration, herein, we put forward an effective strategy through tuning the size of A-site rare-earth (RE) cation in the perovskite structure and successfully synthesize mesoporous $RE(Co_{0.2}Cr_{0.2}Fe_{0.2}Mn_{0.2}Ni_{0.2})O_3$ (RE = La, Sm, and Gd) with obvious lattice distortion as competitive anode materials for LIBs. Attractively, rich oxygen vacancies were simultaneously introduced into the resultant $RE(Co_{0.2}Cr_{0.2}Fe_{0.2}Mn_{0.2}Ni_{0.2})O_3$ samples

by the solution combustion synthesis (SCS) method. Compared with these anode materials, $Gd(Co_{0.2}Cr_{0.2}Fe_{0.2}Mn_{0.2}Ni_{0.2})O_3$ exhibits excellent high-rate capacity and cycling stability due to the synergistic effect of lattice distortion, enriched oxygen vacancies, and mesoporous structure.

2 Experimental

2. 1 Synthesis of $RE(Co_{0.2}Cr_{0.2}Fe_{0.2}Mn_{0.2}Ni_{0.2})O_3$

Perovskite-type $RE(Co_{0.2}Cr_{0.2}Fe_{0.2}Mn_{0.2}Ni_{0.2})O_3$ (RE = La, Sm, and Gd) nanocrystalline powders were fabricated using the SCS method, as predicted in Ref. [25]. Analytical-grade metal nitrates, ($La(NO_3)_3 \cdot 6H_2O$, $Sm(NO_3)_3 \cdot 6H_2O$, $Gd(NO_3)_3 \cdot 6H_2O$, $Co(NO_3)_2 \cdot 6H_2O$, $Cr(NO_3)_3 \cdot 9H_2O$, $Fe(NO_3)_3 \cdot 9H_2O$, $Mn(NO_3)_2 \cdot 4H_2O$, and $Ni(NO_3)_2 \cdot 6H_2O$), and glycine ($C_2H_5NO_2$) fuel (Sinopharm Chemical Reagent Co., Ltd., Beijing, China) were used as the starting materials. Stoichiometric amounts of the above-mentioned agents were dissolved in a minimum amount of deionized water, and then the obtained homogenous solution was dried overnight at 343 K to eliminate the excess water. After that, the obtained gel in a quartz boat was placed in an electric-heated semi-transparent horizontal gold furnace (TF-0410301, Ishikawa-sangyo Co., Ltd.), which was preheated to the setting temperature of 1023 K under an air atmosphere. The combustion reaction was ignited at once, and after further calculated for 30 min, the as-synthesized sample was quenched to room temperature by directly taking out from the hot zone. The reaction between nitrates and fuel is given by Reaction (1):

$$M^x(NO_3)_x + \frac{5}{4}x(\phi-1)O_2 + \frac{5}{9}x\phi C_2H_5NO_2 \rightarrow$$

$$M^xO_{x/2} + \frac{25}{18}x\phi H_2O + x\left(\frac{5\phi+9}{18}\right)N_2 + \frac{10}{9}x\phi CO_2 \quad (1)$$

where M^x indicates the x-valent metal ions, and ϕ implies the ratio of fuel to nitrate, which is maintained at 0.5 in our experiments [26]. Finally, the as-prepared sample was collected, washed twice with ethanol (Sinopharm Chemical Reagent Co., Ltd., Beijing, China), and then dried at 353 K overnight. For convenience, the samples were labeled as $RE(5B_{0.2})O_3$.

2. 2 Physicochemical characterization

The crystal structure, of the as-synthesized samples was

studied using the X-ray diffractometer (Mini-Flex 600, Rigaku), and the X-ray diffraction (XRD) pattern was collected in the rang of $2\theta = 10°$–$80°$ with a step size of $0.02°$ and a scan rate of 2 (°)·min^{-1}. The morphological and microstructural analyses were characterized by the transmission electron microscope (TEM; JEM-2100, JEOL) and the scanning electron microscope (SEM; S-3500N, Hitachi) equipped with an energy dispersive spectrometer (EDS; XFlash Detector 5010, Brukker). The nitrogen (N_2) adsorption/desorption isotherms were obtained on a micromeritics analyzer (TriStar II 3020, Micromeritics) at 77 K to examine the specific surface area and pore diameter distribution, which were calculated by the Brunauer–Emmett–Teller (BET) and Barrett–Joyner–Halenda (BJH) methods, respectively. The surface chemical states of metal cations and the deficiencies of oxygen were investigated using an X-ray photoelectron spectrometer (K-Alpha, Thermo Fisher Scientific). The quantitative multi-element analysis was determined by the inductively coupled plasma-atomic emission spectrometer (ICP-AES; UltraMass 725, Varian). The electron paramagnetic resonance (EPR) spectra were determined by an EPR spectrometer (EMX-plus X, Bruker) at room temperature. The electronic conductivity was obtained by a four-point probe (RTS-4, Guangzhou 4Probes Tech. Ltd.) at 25 ℃ by coating the well-mixed slurry on a plastic substrate.

2. 3 Coin cell assembly and electrochemical characterization

The electrochemical properties were evaluated using coin-type half cells (CR2025, Neware Technology Limited), which were operated in an argon-filled glovebox (Lab 2000, Etelux) using lithium foil as the counter electrode, 1 M $LiPF_6$ in ethylene carbonate (EC)/diethyl carbonate (DEC)/dimethyl carbonate (DMC) by a volume ratio of 1∶1∶1 as the electrolyte, and the microporous polyethylene membrane (Celgard 2400, Celgard, LLC) as a separator. The working electrodes with 15 mm in diameter and 1.5±0.1 mg in mass loading were fabricated by coating the well-mixed slurry on a Cu current collector, as described in Refs. [27,28]. The slurry consisted of the as-synthesized HEO powders (70 wt%), Super P carbon black (20 wt%), and polyvinylidene fluoride (PVDF) binder (10 wt%) in the N-methyl-2-pyrrolidone (NMP) solvent.

The galvanostatic discharge/charge measurements were implemented on a multichannel battery testing system (CT-4008T-5V10mA-164, Neware Technology Limited) over the potential range of 0.01–3.00 V (vs. Li^+/Li). The electrochemical impedance spectroscopy (EIS) and cyclic voltammetry (CV) curves were all performed on an electrochemical workstation (CHI760E, Shanghai Chenhua Instruments Co., China). The EIS analysis was executed over the frequency range between 0.01 and 1.0×10^5 Hz, while the CV curves were scanned over a potential range of 0.01–3.00 V (vs. Li^+/Li) with a scan rate (v) of 0.1, 0.2, 0.5, 0.8 and 1.0 mV·s^{-1}.

3 Results and discussion

3. 1 Material characterization

The XRD patterns of the as-synthesized samples prepared at 1023 K are depicted in Fig. 1(a). Obviously to see that the synthesized three samples exhibit a single-phase perovskite structure with the *Pbnm*(62) space group [29,30]. All the diffraction peaks of $La(5B_{0.2})O_3$, $Sm(5B_{0.2})O_3$, and $Gd(5B_{0.2})O_3$ samples are consistent well with those of $LaNiO_3$ (JCPDS No. 33-0710), $SmNiO_3$ (JCPDS No. 51-0391), and $GdCrO_3$ (JCPDS No. 25-1056), respectively. Furthermore, the Rietveld refinement XRD patterns were carried out using the software package PDXL(5) developed by Rigaku, and the corresponding spectra and obtained parameters from the Rietveld analysis are given in Figs. 1(b)–1(d) and Table 1. Obviously, the observed diffraction pattern is in good agreement with the fitted pattern, except for a slight shift of peak position and slight change in signal intensity due to the solid solubility of five TM cations in B-site [31]. As seen in Table 1, the lattice parameters (a, b, and c) increase with the increase of RE^{3+} radius, and the expanded cell volume is beneficial for the rapid migration of Li-ion during the charge/discharge process, especially at low specific currents [32,33]. Moreover, the crystallite sizes (D) estimated from the most intense XRD peak by the Scherrer's equation are 17.0, 19.6, and 24.8 nm for $La(5B_{0.2})O_3$, $Sm(5B_{0.2})O_3$, and $Gd(5B_{0.2})O_3$, respectively, which are in good agreement with the results of the XRD Rietveld refinement. It should be noted that the smaller the D, the shorter the Li^+ diffusion distance, and the bigger the electrode–electrolyte interface area [34].
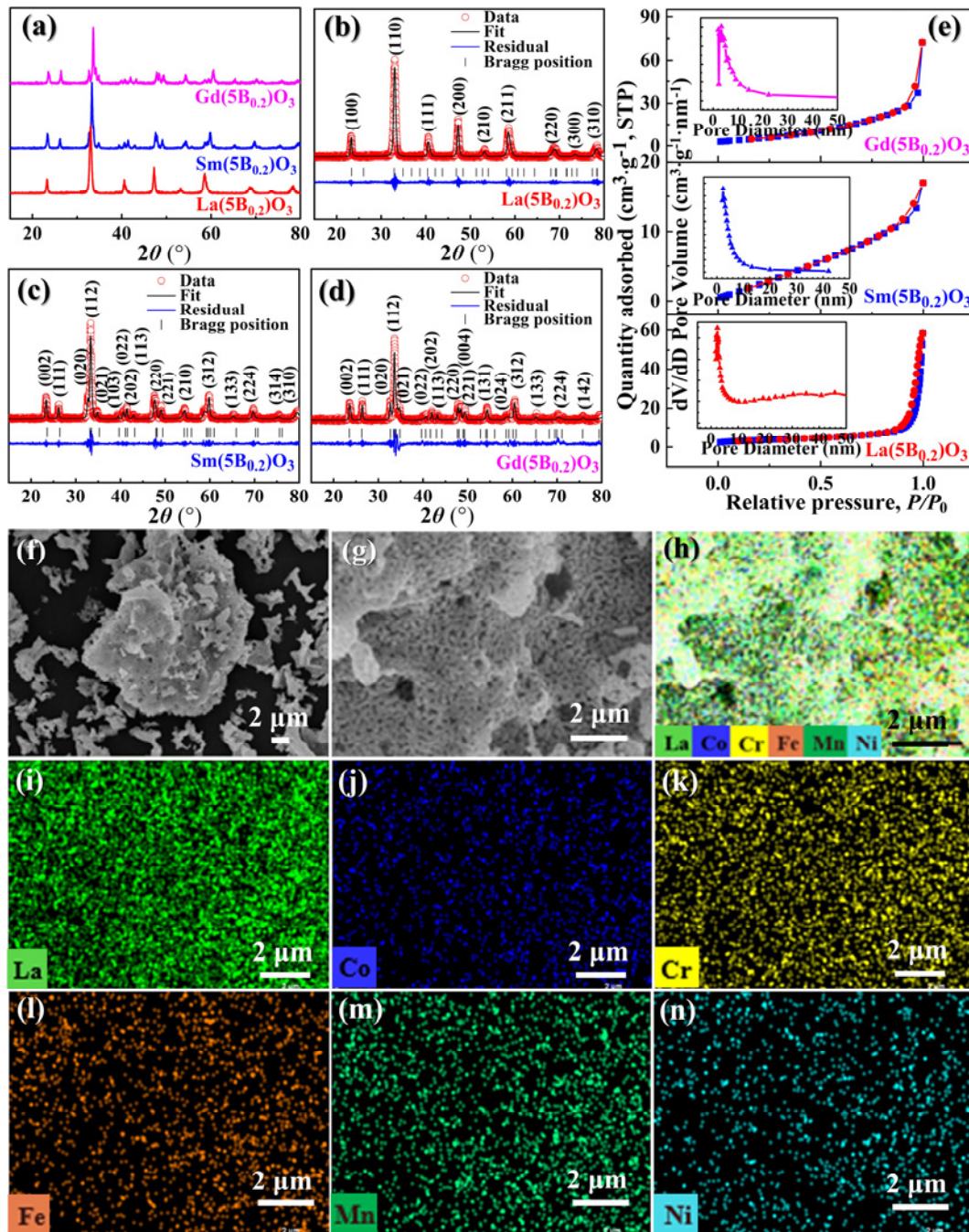
Fig. 1 Structural studies of RE(5B$_{0.2}$)O$_3$: (a–d) XRD patterns and corresponding Rietveld-refined fittings; (e) N$_2$ adsorption/ desorption isotherms together with pore diameter distribution curves; (f, g) SEM images at different magnifications, and (h–n) corresponding elemental mappings of representative La(5B$_{0.2}$)O$_3$ sample.

Table 1   *a*, *b*, and *c*, theoretical densities (ρ), unit cell volumes (*V*), *D*, refinement factors (weighted profile *R*-factor (R_{wp}) and profile *R*-factor (R_p)), RE^{3+} radii, and tolerance factors (*t*) of the as-synthesized samples

Sample	RE^{3+} radius (Å)	*t*	Lattice parameter (Å)			*V* (Å^3)	ρ (g·cm^{-3})	*D* (nm)	Refinement factor	
			a	*b*	*c*				R_{wp} (%)	R_p (%)
La(5B$_{0.2}$)O$_3$	1.36	0.963	5.586	5.527	7.852	242.422	6.65	17.0	2.35	1.75
Sm(5B$_{0.2}$)O$_3$	1.24	0.921	5.329	5.471	7.599	221.55	7.71	19.6	2.87	2.01
Gd(5B$_{0.2}$)O$_3$	1.10	0.900	5.220	5.466	7.589	216.53	8.10	24.8	3.17	2.28

Note: The coordination number (CN) of RE^{3+} is 12.

The quality of the refined XRD pattern is also verified by the R_{wp} and R_p (Table 1). Generally, the smaller the R_{wp} value, the closer the fitted sample structure to the standard crystal structure, and the smaller the lattice distortion [35]. Furthermore, the Goldschmit's t is also used to evaluate the distortion or degree of symmetry of the perovskite, and can be calculated by Eq. (2), where r_A and r_O represent the ionic radii of A-site RE cation and oxygen, respectively; and r_B represent the average ionic radius of multiple cations in B-site. When CN = 6, the ionic radii of Co^{3+}, Cr^{3+}, Fe^{3+}, Mn^{3+}, Ni^{3+}, and O^{2-} are 0.61 Å (high spin (HS)), 0.61 Å, 0.64 Å (HS), 0.64 Å (HS), 0.60 Å (HS), and 1.4 Å, respectively [29,30]. Therefore, the calculated r_B is 0.62 Å. As clearly seen in Table 1, the decrease of RE^{3+} radius in A-site decreases the value of t, and the reduced t in turn leads to the increased lattice distortion. Meanwhile, the lattice distortion of the HEO material itself can also offer additional ion/electron transport pathways, thus improving the electrochemical properties [18].

$$t = (r_A + r_O)/[\sqrt{2}\,(r_B + r_O)] \qquad (2)$$

It has been demonstrated that the specific surface area and porous structure of electrode materials have great influence on the electrochemical properties [14]. Figure 1(e) illustrates the N_2 adsorption/desorption isotherms and BJH pore diameter distribution of the obtained samples. Obviously, all the isotherms belong to Type IV isotherms with Type H3 hysteresis loops, showing the mesoporous characteristics [27,28]. The pore diameter distribution covers the mesoporous region (2–50 nm), which also confirms that the sample contains a rich mesoporous structure. As shown in Table 2, among the three crystalline powders, $Gd(5B_{0.2})O_3$ possesses the highest S_{BET} (21.07 $m^2 \cdot g^{-1}$), the biggest V_{BJH} (0.122 $cm^3 \cdot g^{-1}$), and moderate $D_{aver.}$ (15.60 nm). The high specific surface area and the rich mesoporous structure not only increase the contact area of active material/electrolyte and provide abundant passageway for electron/ion diffusion, but also provide sufficient space for accommodating volume expansion, thus

Table 2 BET specific surface areas (S_{BET}), BJH adsorption cumulative pore volumes (V_{BJH}), and average pore diameters ($D_{aver.}$)

Sample	S_{BET} ($m^2 \cdot g^{-1}$)	V_{BJH} ($cm^3 \cdot g^{-1}$)	$D_{aver.}$ (nm)
$La(5B_{0.2})O_3$	12.25	0.081	28.73
$Sm(5B_{0.2})O_3$	14.17	0.034	5.82
$Gd(5B_{0.2})O_3$	21.07	0.122	15.60

leading to excellent cycle capability and superior rate capability [14,36].

Figures 1(f)–1(n) depict the micrographs and elemental distributions of the representative $La(5B_{0.2})O_3$ sample. Notably seen in the low-magnification landscape image (Fig. 1(f)), the as-synthesized sample consists of granule-like agglomerates with porous microstructures due to the volatilized gas formed during the synthetic process, which is also confirmed by the higher-magnification SEM image (Fig. 1(g)) [28,37,38]. In addition, the energy dispersive spectroscopy (EDS) mappings (Figs. 1(i)–1(n)) demonstrate the microstructral and chemical homogeneity of the as-synthesized $La(5B_{0.2})O_3$ sample. Furthermore, the atomic ratio of La : Co : Cr : Fe : Mn : Ni in $La(5B_{0.2})O_3$ sample determined by the ICP-AES is 1.0 : 0.19 : 0.21 : 0.20 : 0.18 : 0.22, which is very close to the stoichiometric ratio in the chemical formula.

To study the surface chemical states of the elements, the X-ray photoelectron spectroscopy (XPS) analysis was performed on the as-synthesized samples, as presented in Figs. 2(a)–2(g). The results suggest that the RE, Co, and Cr cations in $RE(5B_{0.2})O_3$ samples are in the trivalent states, while the Fe, Ni, and Mn cations exhibit mixed divalent/trivalent states. As highlighted in Fig. 2(b), the spectra of Co 2p consist of Co $2p_{3/2}$ peak at 779.6 eV and Co $2p_{1/2}$ peak at 795.0 eV, which can be indexed to Co^{3+} species [13,27]. While the peaks located at 790.2 and 806.3 eV correspond to the satellite peaks (S1 and S2) of Co $2p_{3/2}$ and Co $2p_{1/2}$, respectively. Similarly, the Cr $2p_{3/2}$ and Cr $2p_{1/2}$ peaks at 576.1 and 586.1 eV with the corresponding satellite peaks at 579.2 and 588.4 eV can be identified as the Cr^{3+} species (Fig. 2(c)) [39]. For the Fe 2p spectra (Fig. 2(d)), the fitted peaks at 709.9 eV (Fe $2p_{3/2}$) and 723.3 eV (Fe $2p_{1/2}$) are attributed to Fe^{2+}, and the peaks at 712.1 eV (Fe $2p_{3/2}$) and 725.0 eV (Fe $2p_{1/2}$) are indexed to Fe^{3+} [39]. Figure 2(e) depicts the spectra of Mn 2p, and the Mn $2p_{3/2}$ spectra are split to Mn^{2+} at 641.6 eV and Mn^{3+} at 642.7 eV, while the divided Mn $2p_{1/2}$ spectra at 653.4 and 655.7 eV are the characteristic peaks of Mn^{2+} and Mn^{3+}, respectively [40]. The spectra of Ni 2p (Fig. 2(f)) consist of two intense peaks and an obvious shoulder peak (S), and the fitted peaks located at 850.4 and 854.2 eV correspond to Ni^{2+} and Ni^{3+}, respectively [41]. The O 1s binding energies located at 528.9, 531.1, and 532.7 eV are ascribed to the lattice oxygen (O_L), O_V, and surface adsorbed oxygen (O_S), respectively [13,39,42,43]. The calculated O_V/O_L ratio
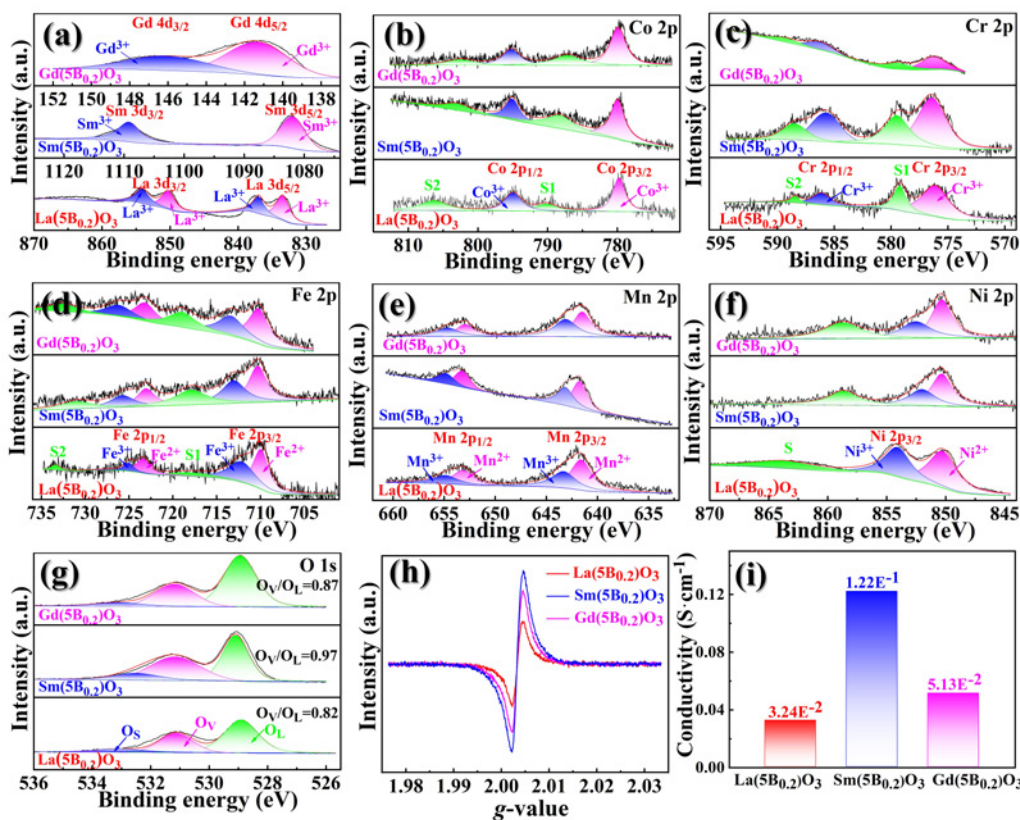
Fig. 2 High-resolution XPS spectra of (a) RE, (b) Co 2p, (c) Cr 2p, (d) Fe 2p, (e) Mn 2p, (f) Ni 2p, and (g) O 1s; (h) EPR spectra of RE(5B$_{0.2}$)O$_3$; and (i) electrical conductivity of RE(5B$_{0.2}$)O$_3$.

of La(5B$_{0.2}$)O$_3$ according to the peak area is about 0.82, followed by 0.87 of Ga(5B$_{0.2}$)O$_3$ and 0.97 of Sm(5B$_{0.2}$)O$_3$, clearly confirming that the content of oxygen vacancies in Gd(5B$_{0.2}$)O$_3$ is in the middle of the as-synthesized three samples.

Furthermore, the EPR was also conducted to investigate the oxygen vacancies through the *g*-value that is the characteristic for unpaired electrons in the as-synthesized crystals. As shown in Fig. 2(h), all three samples exhibit strong EPR signal in a value of 2.003, which is related to the unpaired electrons caused by the oxygen deficiency [4,44,45]. Note that Gd(5B$_{0.2}$)O$_3$ has a middle EPR intensity value among the three samples, suggesting the moderate oxygen vacancies in Gd(5B$_{0.2}$)O$_3$, which agrees well with the result obtained from the O 1s XPS spectra. Furthermore, the electronic conductivity of the three samples was characterized by the four-point probe resistance measurement (Fig. 2(i)). Obviously, the Sm(5B$_{0.2}$)O$_3$ with the highest O$_V$ delivers the highest electronic conductivity of 0.122 S·cm^{-1} at room temperature. It has been demonstrated that the rich oxygen vacancies can effectively increase the electric conductivity, and act as active sites for fast electrochemical reactions, thus significantly improving

the rate capability and cycling performance [4,24,46–48]. However, excessive O$_V$ will lead to the accelerated degradation of electrode material structure, and thereby the battery properties [49].

3.2 Electrochemical evaluation

To better understand the transformation mechanism of all three RE(5B$_{0.2}$)O$_3$ electrodes during the charge/discharge process, the initial three CV curves of RE(5B$_{0.2}$)O$_3$ electrodes at *v* = 0.1 mV·s^{-1} under 0.01–3.00 V are presented in Figs. 3(a)–3(c). It is noted that the CV curves are similar, indicating that the RE ionic replacement in A-site of the three electrodes does not change the redox reaction process. For the first cycle, the obvious irreversible cathodic peaks located at ~1.60/1.57/1.60 V disappear in the subsequent cycles, which can be attributed to the electrolyte decomposition and solid electrolyte interphase (SEI) formation. While the cathodic peaks observed at 0.33/0.42/0.31 V are ascribed to the further reduction of TM ions to the corresponding Co^0, Cr^0, Fe^0, Mn^0, and Ni^0 accompanied by Li$_2$O formation [50]. In subsequent cycles, the reduction peaks shift to the higher potentials and become broader due to the

pulverization of the electrode [51]. While the two oxidation peaks for the corresponding electrodes are found to be virtually unchanged during the subsequent cycles, and can be ascribed to the oxidation of metallic Co^0, Cr^0, Fe^0, Mn^0, and Ni^0, accompanying the decomposition of Li_2O [52]. All the cathodic and anodic curves almost overlap after the first cycle, suggesting favorable electrochemical reversibility during the Li^+ insertion/extraction process. Note that the potential difference ($\Delta\varphi$) between the anodic and cathodic peaks of La(5B$_{0.2}$)O$_3$ electrode is the smallest, followed by the Gd(5B$_{0.2}$)O$_3$ and Sm(5B$_{0.2}$)O$_3$ electrodes, suggesting the reduced polarization and improved reversibility of La(5B$_{0.2}$)O$_3$ electrode [13,53].

Figures 3(d)–3(f) display the first three discharge/charge curves of RE(5B$_{0.2}$)O$_3$ electrodes. As expected, a short voltage plateau at a high potential and a long potential plateau at a low potential can be clearly observed during the first discharge. The former discharge plateau disappeared from the second discharge process onward corresponds to the SEI formation, whereas the latter potential plateau is related to the reversible reduction reaction. During the charge process, all the charge curves show a continuously increasing potential slope to ~2.5 V, corresponding to the reversible oxidation reaction. The results of discharge/charge profiles are well consistent with those of the CV studies. Furthermore, the La(5B$_{0.2}$)O$_3$ electrode shows the highest initial discharge capacity of 663 mAh·g^{-1} and initial coulombic efficiency (ICE) of 66.5%, in contrast with Sm(5B$_{0.2}$)O$_3$ (457 mAh·g^{-1} and 49.5%) and Gd(5B$_{0.2}$)O$_3$ (493 mAh·g^{-1} and 50.5%). The maximum specific capacity of La(5B$_{0.2}$)O$_3$ at 0.2 A·g^{-1} may be attributed to the expanded cell volume, which can provide a broadening channel for the transportation of Li^+ and avoid the volume expansion during the Li^+ insertion/extraction process, especially at low specific currents [33].

The cycling behaviors of the as-synthesized three electrodes are evaluated at 0.2 A·g^{-1}, as presented in Fig. 3(g). All the electrodes show a significant decay in the specific capacity during the initial two cycles due to the SEI formation and irreversible Li^+ trapping. With the progressively increasing cycle numbers, the specific capacities gradually increase owing to the gradual activation process of the electrode materials,
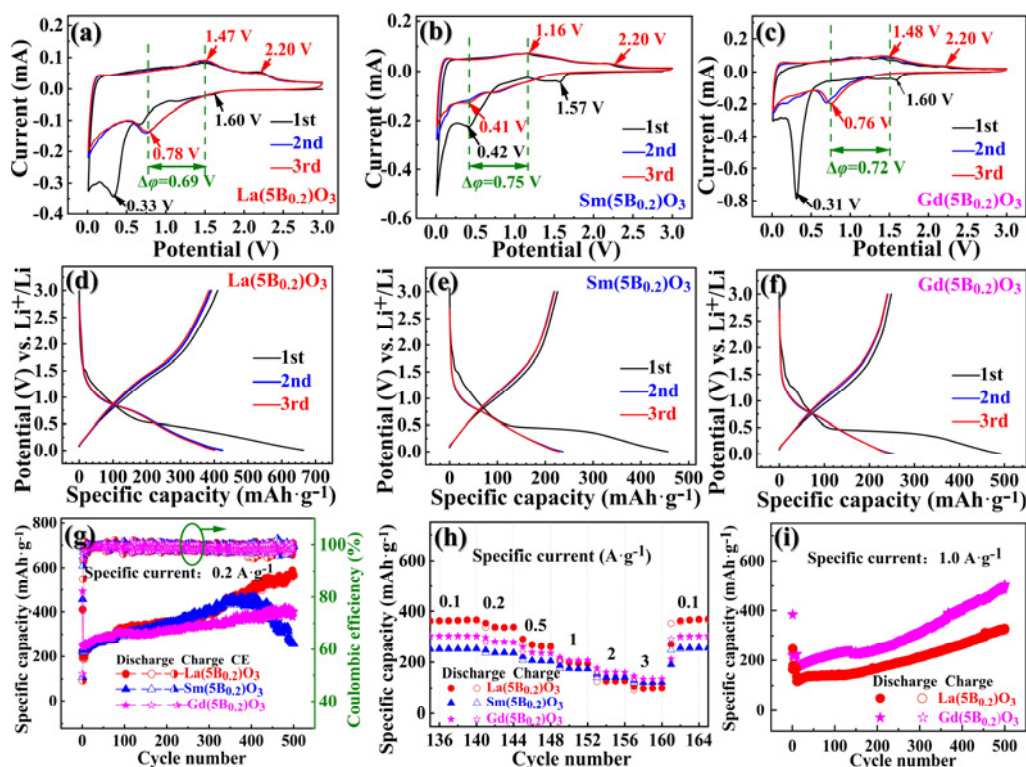

Fig. 3 Electrochemical performance of RE(5B$_{0.2}$)O$_3$: CV curves of (a) La(5B$_{0.2}$)O$_3$, (b) Sm(5B$_{0.2}$)O$_3$, and (c) Gd(5B$_{0.2}$)O$_3$ electrodes at 0.1 mV·s^{-1}; discharge/charge profiles of (d) La(5B$_{0.2}$)O$_3$, (e) Sm(5B$_{0.2}$)O$_3$, and (f) Gd(5B$_{0.2}$)O$_3$ electrodes at 0.2 A·g^{-1}; (g) cycling performance together with corresponding coulombic efficiency of three electrodes at 0.2 A·g^{-1}; (h) rate capabilities after activation process; and (i) high-rate cycling performance of La(5B$_{0.2}$)O$_3$ and Gd(5B$_{0.2}$)O$_3$ electrodes at 1.0 A·g^{-1} with ten initial cycles at 0.2 A·g^{-1}.

which was further confirmed by the refined particles of the as-synthesized electrode material during cycling (Fig. 4). A similar phenomenon is also discovered in rock-salt-type $(Co_{0.2}Cu_{0.2}Mg_{0.2}Ni_{0.2}Zn_{0.2})O$ [1,11,12,54] and spinel-type HEO anodes [13,27,34]. Nevertheless, for the $Sm(5B_{0.2})O_3$ electrode, a noticeable capacity degradation after 400 cycles is clearly observed, which may be caused by the degradation of electrode material structure due to the excessive O_V (Fig. 2(g)) [49]. While for $La(5B_{0.2})O_3$ and $Gd(5B_{0.2})O_3$ electrodes, there is also a small downward trend of capacity at the end of the cycle. It is apparently found that the $La(5B_{0.2})O_3$ electrode delivers the highest specific capacity during the discharge/charge cycling tests, and the reversible specific capacities of $La(5B_{0.2})O_3$, $Sm(5B_{0.2})O_3$, and $Gd(5B_{0.2})O_3$ electrodes are 569, 258, and 403 $mAh \cdot g^{-1}$ at 0.2 $A \cdot g^{-1}$ after 500 cycles, respectively. The theoretical specific capacity can be calculated by Eq. (3), where n (= 3 for the as-synthesized samples) is the number of elections per molecule in the redox reaction, and F (= 96,485 $C \cdot mol^{-1}$) and M represent the Faraday constant and molar mass, respectively. Therefore, the calculated theoretical specific capacities are 330.9, 316.0, and 307.7 $mAh \cdot g^{-1}$ for $La(5B_{0.2})O_3$, $Sm(5B_{0.2})O_3$, and $Gd(5B_{0.2})O_3$ electrodes, respectively. Obviously, the actual specific capacities of $La(5B_{0.2})O_3$ and $Gd(5B_{0.2})O_3$ electrodes are higher than their theoretical specific capacities due to their high pseudo-capacitive behavior, which contributes an additional interfacial capacity (Fig. 5) [15,16].

$$Capacity = \frac{nF}{3.6M} \tag{3}$$

In order to eliminate the influence of electrode activation on the electrochemical behavior, the rate capabilities of $RE(5B_{0.2})O_3$ electrodes from 0.1 to 3.0 $A \cdot g^{-1}$ were tested between 135 and 165 cycles, as shown in Fig. 3(h). Progressively increasing the current density, the specific capacity fades continuously. While the current density decreases back to 0.1 $A \cdot g^{-1}$, the capacities are restored to 371, 256, and 300 $mAh \cdot g^{-1}$ for $RE(5B_{0.2})$ (RE = La, Sm, and Gd, respectively). Note that $La(5B_{0.2})O_3$ electrode exhibits the highest specific capacities at 0.1, 0.2, and 0.5 $A \cdot g^{-1}$ due to the largest cell volume, which is beneficial to the improvement of capacity at a lower rate; while for $Gd(5B_{0.2})O_3$ electrode, it delivers the highest specific capacities at higher rates of 1.0, 2.0, and 3.0 $A \cdot g^{-1}$ due to the increased lattice distortion and richer oxygen vacancies, which can simultaneously promote the rapid transport of Li^+ and electron. Furthermore, due to the instability of the cycling performance of the $Sm(5B_{0.2})O_3$ electrode at 0.2 $A \cdot g^{-1}$, we only investigated the high-rate cycling performance of $La(5B_{0.2})O_3$ and $Gd(5B_{0.2})O_3$ electrodes at a high current density of 1.0 $A \cdot g^{-1}$, as shown in Fig. 3(i). $Gd(5B_{0.2})O_3$ electrode still delivers the higher reversible capacity of 394 $mAh \cdot g^{-1}$ after 500 charge/discharge cycles, in contrast with $La(5B_{0.2})O_3$ electrode (325 $mAh \cdot g^{-1}$).

As summarized in Table 3, such a high-rate capacity achieved by $Gd(5B_{0.2})O_3$ electrode is superior to those of some other published perovskite-type anode materials,

Table 3   Comparison of lithium-ion storage properties of perovskite-type anodes

Composition	Method	Capacity at 0.1 $A \cdot g^{-1}$ ($mAh \cdot g^{-1}$)	Rate capability ($mAh \cdot g^{-1}$)	Cycling performance ($mAh \cdot g^{-1}$) (cycles)	Ref.
$Gd(Co_{0.2}Cr_{0.2}Fe_{0.2}Mn_{0.2}Ni_{0.2})O_3$	SCS	300	207 at 2.0 $A \cdot g^{-1}$; 135 at 3.0 $A \cdot g^{-1}$	403 (500) at 0.2 $A \cdot g^{-1}$; 394 (500) at 1.0 $A \cdot g^{-1}$	This work
$La(Co_{0.2}Cr_{0.2}Fe_{0.2}Mn_{0.2}Ni_{0.2})O_3$	SCS	371	197 at 2.0 $A \cdot g^{-1}$; 100 at 3.0 $A \cdot g^{-1}$	569 (500) at 0.2 $A \cdot g^{-1}$; 325 (500) at 1.0 $A \cdot g^{-1}$	This work
$La(Co_{0.2}Cr_{0.2}Fe_{0.2}Mn_{0.2}Ni_{0.2})O_3$	Coprecipitation	450	350 at 3.0 $A \cdot g^{-1}$	772 (150) at 0.2 $A \cdot g^{-1}$; 320 (500) at 3.0 $A \cdot g^{-1}$	[56]
$[(Bi,Na)_{1/5}(La,Li)_{1/5}(Ce,K)_{1/5}Ca_{1/5}Sr_{1/5}]TiO_3$	Mechanochemical	84	59 at 3.0 $A \cdot g^{-1}$	115 (300) at 1.0 $A \cdot g^{-1}$	[23]
$Li_{0.1}(LiLaCaSrBa)Ti_{0.9}Al_{0.1}O_3$	Mechanochemical	59	37 at 1.0 $A \cdot g^{-1}$	57 (100) at 0.1 $A \cdot g^{-1}$	[55]
$LaMO_3$ (M = Fe, Co, and Ni) nanofibers	Electrospinning approach	150 at 0.2 $A \cdot g^{-1}$ for $LaCoO_3$	150 at 2.0 $A \cdot g^{-1}$ for $LaCoO_3$	331, 646, and 92 (200) at 0.2 $A \cdot g^{-1}$ for $LaFeO_3$, $LaCoO_3$, and $LaNiO_3$, respectively	[22]
$LaCoO_3/Co_3O_4$-800	Hydrothermal method	564.4	333 at 1.0 $A \cdot g^{-1}$; 263 at 2.0 $A \cdot g^{-1}$	550 (100) at 0.1 $A \cdot g^{-1}$; 397 (1000) at 1.0 $A \cdot g^{-1}$	[50]
$Nd_{0.7}Co_{0.3}FeO_3$	Hydrothermal method	—	—	291 (100) at 0.5 $A \cdot g^{-1}$	[57]
$CaMnO_3$	Liquid phase synthesis method	101.3	26.7 at 1.0 $A \cdot g^{-1}$	107.2 (70) at 0.1 $A \cdot g^{-1}$	[58]

such as $[(Bi,Na)_{1/5}(La,Li)_{1/5}(Ce,K)_{1/5}Ca_{1/5}Sr_{1/5}]TiO_3$ HEO [23], $Li_{0.1}(LiLaCaSrBa)Ti_{0.9}Al_{0.1}O_3$ HEO [55], and $LaCoO_3$ nanofiber [22], except for $La(Co_{0.2}Cr_{0.2}Fe_{0.2}Mn_{0.2}Ni_{0.2})O_3$ electrode synthesized by the coprecipitation method [56]. Although the high-rate cyclic capacity of $Gd(5B_{0.2})O_3$ electrode is equivalent to that of $LaCoO_3/Co_3O_4$-800 (397 mAh·g^{-1} after 1000 cycles at 1.0 A·g^{-1}) [50], it is conductive to reducing the content of cobalt and breaking the reliance on high-cost cobalt.

In order to investigate the influence of oxygen vacancies on the stability of electrode structure, the structural changes of the three electrodes after 500 cycles at 0.2 A·g^{-1} were characterized by the SEM and TEM/ high-resolution TEM (HRTEM). As shown in Figs. 4(a)–4(c), the $La(5B_{0.2})O_3$ and $Gd(5B_{0.2})O_3$ electrodes with long-term cycling performance deliver excellent structural integrity even after 500 cycles. However, for the $Sm(5B_{0.2})O_3$ electrode, it suffers from serious

agglomeration problem, which leads to the reduction of active sites and structural instability of the electrode.

Furthermore, the morphological and structural evolution of representative $La(5B_{0.2})O_3$ was also systematically studied via the TEM analysis to elucidate the electrochemical mechanism, as presented in Figs. 4(d)–4(g). Compared with that of the original $La(5B_{0.2})O_3$, the morphology remains almost unchanged, and the particle size becomes smaller after cycling. Recently, Wang *et al.* [59] first reported that the micron-sized $(Co_{0.2}Cu_{0.2}Mg_{0.2}Ni_{0.2}Zn_{0.2})O$ anode material turned into a composite with intrinsic semi-coherent metal/oxide nanophases after the 1st discharging. It is well known that the small particles not only provide more interface area for contact with electrolyte, but also can shorten the Li$^+$ diffusion distance and electron transport path, thus providing more active sites and increasing the specific capacity [60,61]. The high-resolution TEM (HRTEM) and selected-area electron
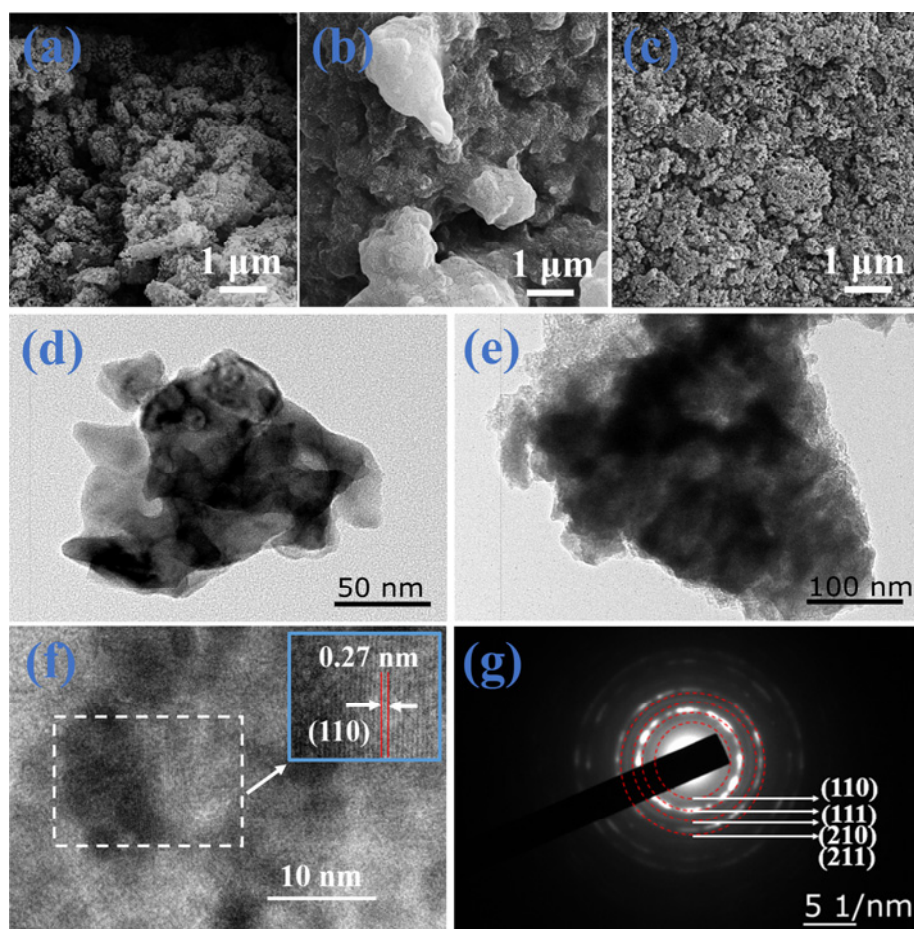

Fig. 4 SEM images of (a) $La(5B_{0.2})O_3$, (b) $Sm(5B_{0.2})O_3$, and (c) $Gd(5B_{0.2})O_3$ electrodes after 500 cycles; (d) TEM image of $La(5B_{0.2})O_3$ before cycle; and (e) TEM image, (f) high-resolution lattice image, and (g) SAED pattern of $La(5B_{0.2})O_3$ after 500 cycles.

diffraction (SAED) results (Figs. 4(f) and 4(g), respectively) confirm that the perovskite structure of La(5B$_{0.2}$)O$_3$ electrode is maintained even after 500 cycles. The measured interplanar spacing between the adjacent lattice fringe is 0.27 nm, consistent with the (110) crystal plane distance of the perovskite structure. Meanwhile, the discontinuous diffraction rings (Fig. 4(g)) can be well indexed to the (110), (111), (210), and (211) planes of the perovskite structure, which agrees well with the XRD data. Therefore, we can conclude that the moderate oxygen vacancies and the high-entropy stabilization effects in La(5B$_{0.2}$)O$_3$ and Gd(5B$_{0.2}$)O$_3$ are crucial for promoting the electrode cycling stability.

3.3 Kinetics analysis

To further elucidate the lithium-ion storage mechanism and the kinetics process of La(5B$_{0.2}$)O$_3$ and Gd(5B$_{0.2}$)O$_3$ electrodes, the CV determinations were measured at different v in the voltage range of 0.01–3.00 V. As highlighted in Figs. 5(a1) and 5(a2), the CV curves show the similar shapes, and the peak current (i_p) increases with the increasing v. It is well known that the i_p and v obey the relationship based on $i_p = av^b$, where the parameters a and b can be quantitatively obtained from the equation of $\log i_p = b\log v + \log a$. The parameter b offers the insight into the lithium-ion storage mechanism. When $b = 1$ indicates a typical
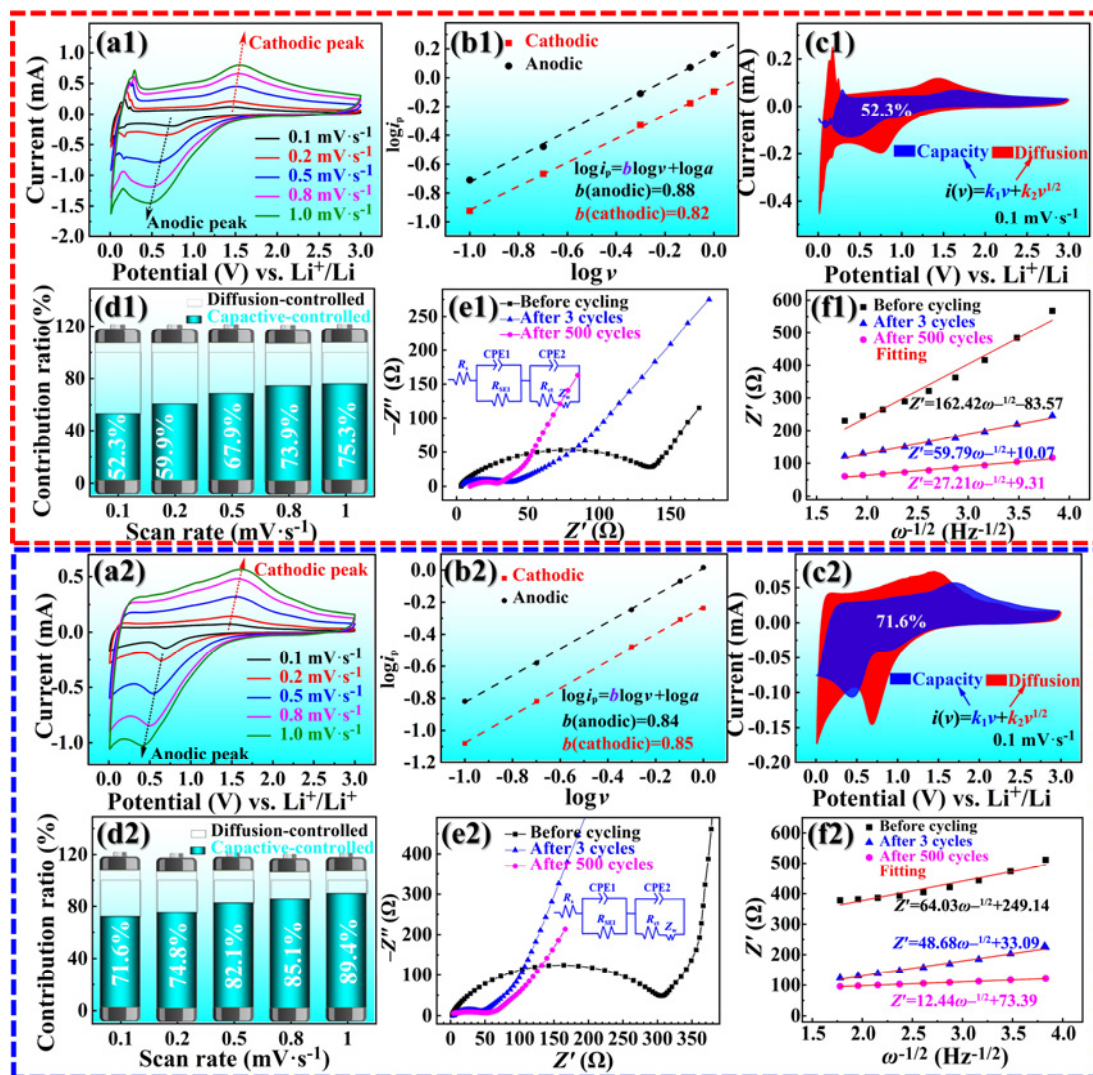

Fig. 5 Kinetics analysis of (a1–f1) La(5B$_{0.2}$)O$_3$ and (a2–f2) Gd(5B$_{0.2}$)O$_3$ electrodes: (a1, a2) CV curves under various v; (b1, b2) determination of b value using the corresponding $\log i_p$ and $\log v$; (c1, c2) separation of capacitive- (the blue region) and diffusion- (the red region) controlled contribution at 0.1 mV·s^{-1}; (d1, d2) contribution ratios of capacitive- and diffusion-controlled processes at different v; (e1, e2) Nyquist plots (imaginary impedance (Z'') versus real impedance (Z')) together with equivalent circuit; and (f1, f2) fitting lines of Z' against $\omega^{-1/2}$ in the low frequency region.

surface capacitive-controlled charge storage process, whereas b = 0.5 implies a diffusion-controlled redox process [13,14]. Obviously seen in Figs. 5(b1) and 5(b2), the values of (slopes for) the anodic and cathodic peaks of La(5B$_{0.2}$)O$_3$ and Gd(5B$_{0.2}$)O$_3$ electrodes, respectively, in principle, demonstrate the mixed redox mechanism of lithium-ion storage [13,62]. The ratio of capacitive contribution can be calculated according to $i_p = k_1v + k_2v^{1/2}$, where k_1v and $k_2v^{1/2}$ represent the capacitive and diffusion behavior, respectively. As shown in Figs. 5(c2) and 5(d2), the capacitive-controlled contribution for Gd(5B$_{0.2}$)O$_3$ electrode is 71.6% at 0.1 mV·s^{-1}, and the ratio increases gradually to 89.4% as the v increases to 1.0 mV·s^{-1}, higher than that of La(5B$_{0.2}$)O$_3$ electrode (Figs. 5(c1) and 5(d1)), indicating the superior rate capability of Gd(5B$_{0.2}$)O$_3$ electrode.

To deeply explain the origins of the fast reaction kinetics of Gd(5B$_{0.2}$)O$_3$, the EIS measurements were then performed for La(5B$_{0.2}$)O$_3$ and Gd(5B$_{0.2}$)O$_3$ for comparison, as displayed in Figs. 5(e1) and 5(e2), respectively. It should be pointed that the Nyquist profiles contain similar semicircles in high-frequency ranges and slope lines at low-frequency ranges, corresponding to charge transfer dynamics and mass transfer dynamics, respectively [63]. Obviously to see in Figs. 5(e1) and 5(e2) that the semicircle diameter relating to charge-transfer resistance (R_{ct}) decreases as the cycle progresses, confirming the improvement of charge transfer ability over the cycles. Furthermore, as shown in Figs. 5(f1) and 5(f2), the slope of the line, inversely correlating to the Warburg impedance (Z_w), also decreases as the cycle progresses, revealing the increase of Li$^+$ diffusion coefficient (D_{Li^+}) over the cycles [27]. Therefore, the decreased R_{ct} and increased D_{Li^+} over the cycles indicate the improved kinetics of ion and electron transport, which can experimentally explain why the specific capacities of the as-synthesized La(5B$_{0.2}$)O$_3$ and Gd(5B$_{0.2}$)O$_3$ electrodes gradually increase with the cycle progresses after the initial two cycles. Noting in Figs. 5(f1) and 5(f2), the slope of the straight line of Gd(5B$_{0.2}$)O$_3$ is smaller than that of La(5B$_{0.2}$)O$_3$ in the same cycle, suggesting that Gd(5B$_{0.2}$)O$_3$ possesses higher D_{Li^+}. Overall, the rich electrochemical active sites, enhanced electronic conductivity, and desirable Li$^+$ kinetics diffusion make the electrochemical reactions in a fast and highly reversible manner at high current densities, thereby yielding a superior rate capability for Gd(5B$_{0.2}$)O$_3$ electrode.

4 Conclusions

In summary, the as-synthesized single-phase perovskite RE(5B$_{0.2}$)O$_3$ (RE = La, Sm, and Gd) nanocrystalline powders possess a certain degree of lattice distortion and rich oxygen vacancies. Among the as-synthesized three anode materials, the La(Co$_{0.2}$Cr$_{0.2}$Fe$_{0.2}$Mn$_{0.2}$Ni$_{0.2}$)O$_3$ and Gd(Co$_{0.2}$Cr$_{0.2}$Fe$_{0.2}$Mn$_{0.2}$Ni$_{0.2}$)O$_3$ electrodes deliver excellent cycling stability owing to the moderate oxygen vacancies and entropy stabilization effect. Meanwhile, the Gd(Co$_{0.2}$Cr$_{0.2}$Fe$_{0.2}$Mn$_{0.2}$Ni$_{0.2}$)O$_3$ electrode exhibits a reversible capacity of 403 mAh·g^{-1} at 0.2 A·g^{-1} after 500 cycles, and a superior high-rate capacity of 394 mAh·g^{-1} at 1.0 A·g^{-1} after 500 cycles. Such a superior high-rate lithium-ion storage capability of Gd(Co$_{0.2}$Cr$_{0.2}$Fe$_{0.2}$Mn$_{0.2}$Ni$_{0.2}$)O$_3$ can be explained by the synergetic effect of lattice distortion and oxygen vacancies. On the one hand, the moderate oxygen vacancies on the surface of Gd(Co$_{0.2}$Cr$_{0.2}$Fe$_{0.2}$Mn$_{0.2}$Ni$_{0.2}$)O$_3$ can not only accelerate the ionic/electronic diffusion kinetics and provide extra active sites for Li$^+$ storage, but also retain the structural stability of the electrode material, thus achieving superior high-rate lithium-ion storage performance and excellent cycling stability. On the other hand, the lattice distortion in a certain degree can also offer abundant ion transport pathways. In addition, the as-synthesized electrodes demonstrate the mixed redox mechanism of lithium-ion storage, and the increased pseudo-capacitive behavior can obtain an additional capacity. The present work opens a new way to optimize the performance for energy storage application by tailoring the A-site cations in ABO$_3$- type HEOs to generate balanced lattice distortion and oxygen vacancies.

Declaration of competing interest

The authors have no competing interests to declare that are relevant to the content of this article.

References

[1] Sarkar A, Velasco L, Wang D, *et al*. High entropy

oxides for reversible energy storage. *Nat Commun* 2018, **9**: 3400.

[2] Xu YS, Xu X, Bi L. A high-entropy spinel ceramic oxide as the cathode for proton-conducting solid oxide fuel cells. *J Adv Ceram* 2022, **11**: 794–804.

[3] Xiang HM, Xing Y, Dai FZ, *et al*. High-entropy ceramics: Present status, challenges, and a look forward. *J Adv Ceram* 2021, **10**: 385–441.

[4] Zhao J, Yang X, Huang Y, *et al*. Entropy stabilization effect and oxygen vacancies enabling spinel oxide highly reversible lithium-ion storage. *ACS Appl Mater Interfaces* 2021, **13**: 58674–58681.

[5] Yuan K, Tu TZ, Shen C, *et al*. Self-ball milling strategy to construct high-entropy oxide coated $LiNi_{0.8}Co_{0.1}Mn_{0.1}O_2$ with enhanced electrochemical performance. *J Adv Ceram* 2022, **11**: 882–892.

[6] Yan SX, Luo SH, Yang L, *et al*. Novel P2-type layered medium-entropy ceramics oxide as cathode material for sodium-ion batteries. *J Adv Ceram* 2022, **11**: 158–171.

[7] Ning YT, Pu YP, Wu CH, *et al*. Enhanced capacitive energy storage and dielectric temperature stability of A-site disordered high-entropy perovskite oxides. *J Mater Sci Technol* 2023, **145**: 66–73.

[8] Wang YH, Liu JP, Song YF, *et al*. High-entropy perovskites for energy conversion and storage: Design, synthesis, and potential applications. *Small Methods* 2023, https://doi.org/10.1002/smtd.202201138.

[9] Bérardan D, Franger S, Meena AK, *et al*. Room temperature lithium superionic conductivity in high entropy oxides. *J Mater Chem A* 2016, **4**: 9536–9541.

[10] Wang QS, Sarkar A, Li ZY, *et al*. High entropy oxides as anode material for Li-ion battery applications: A practical approach. *Electrochem Commun* 2019, **100**: 121–125.

[11] Qiu N, Chen H, Yang ZM, *et al*. A high entropy oxide $(Mg_{0.2}Co_{0.2}Ni_{0.2}Cu_{0.2}Zn_{0.2}O)$ with superior lithium storage performance. *J Alloys Compd* 2019, **777**: 767–774.

[12] Chen H, Qiu N, Wu BZ, *et al*. Tunable pseudocapacitive contribution by dimension control in nanocrystalline-constructed $(Mg_{0.2}Co_{0.2}Ni_{0.2}Cu_{0.2}Zn_{0.2})O$ solid solutions to achieve superior lithium-storage properties. *RSC Adv* 2019, **9**: 28908–28915.

[13] Wang D, Jiang SD, Duan CQ, *et al*. Spinel-structured high entropy oxide $(FeCoNiCrMn)_3O_4$ as anode towards superior lithium storage performance. *J Alloys Compd* 2020, **844**: 156158.

[14] Chen H, Qiu N, Wu BZ, *et al*. A new spinel high-entropy oxide $(Mg_{0.2}Ti_{0.2}Zn_{0.2}Cu_{0.2}Fe_{0.2})_3O_4$ with fast reaction kinetics and excellent stability as an anode material for lithium ion batteries. *RSC Adv* 2020, **10**: 9736–9744.

[15] Sun Z, Zhao YJ, Sun C, *et al*. High entropy spinel-structure oxide for electrochemical application. *Chem Eng J* 2022, **431**: 133448.

[16] Xiao B, Wu G, Wang TD, *et al*. High-entropy oxides as advanced anode materials for long-life lithium-ion batteries. *Nano Energy* 2022, **95**: 106962.

[17] Lun ZY, Ouyang B, Kwon DH, *et al*. Cation-disordered rocksalt-type high-entropy cathodes for Li-ion batteries. *Nat Mater* 2021, **20**: 214–221.

[18] Yang XB, Wang HQ, Song YY, *et al*. Low-temperature synthesis of a porous high-entropy transition-metal oxide as an anode for high-performance lithium-ion batteries. *ACS Appl Mater Interfaces* 2022, **14**: 26873–26881.

[19] Luo XF, Patra J, Chuang WT, *et al*. Charge–discharge mechanism of high-entropy Co-free spinel oxide toward Li^+ storage examined using operando quick-scanning X-ray absorption spectroscopy. *Adv Sci* 2022, **9**: 2201219.

[20] Ma JX, Chen KP, Li CW, *et al*. High-entropy stoichiometric perovskite oxides based on valence combinations. *Ceram Int* 2021, **47**: 24348–24352.

[21] Nguyen AT, Phung VD, Mittova VO, *et al*. Fabricating nanostructured $HoFeO_3$ perovskite for lithium-ion battery anodes via co-precipitation. *Scripta Mater* 2022, **207**: 114259.

[22] Hu QL, Yue B, Shao HY, *et al*. Facile syntheses of perovskite type $LaMO_3$ (M = Fe, Co, Ni) nanofibers for high performance supercapacitor electrodes and lithium-ion battery anodes. *J Alloys Compd* 2021, **852**: 157002.

[23] Yan JH, Wang D, Zhang XY, *et al*. A high-entropy perovskite titanate lithium-ion battery anode. *J Mater Sci* 2020, **55**: 6942–6951.

[24] Li L, Xie ZJ, Jiang GX, *et al*. Efficient laser-induced construction of oxygen-vacancy abundant nano-$ZnCo_2O_4$/porous reduced graphene oxide hybrids toward exceptional capacitive lithium storage. *Small* 2020, **16**: 2001526.

[25] Mao AQ, Xiang HZ, Zhang ZG, *et al*. A new class of spinel high-entropy oxides with controllable magnetic properties. *J Magn Magn Mater* 2020, **497**: 165884.

[26] Mao AQ, Xie HX, Xiang HZ, *et al*. A novel six-component spinel-structure high-entropy oxide with ferrimagnetic property. *J Magn Magn Mater* 2020, **503**: 166594.

[27] Xiang HZ, Xie HX, Chen YX, *et al*. Porous spinel-type $(Al_{0.2}CoCrFeMnNi)_{0.58}O_{4-\delta}$ high-entropy oxide as a novel high-performance anode material for lithium-ion batteries. *J Mater Sci* 2021, **56**: 8127–8142.

[28] Xiang HZ, Xie HX, Li WC, *et al*. Synthesis and electrochemical performance of spinel-type high-entropy oxides. *Chem J Chinese Universities* 2020, **41**: 1801–1809. (in Chinese)

[29] Sarkar A, Djenadic R, Wang D, *et al*. Rare earth and transition metal based entropy stabilised perovskite type oxides. *J Eur Ceram Soc* 2018, **38**: 2318–2327.

[30] Witte R, Sarkar A, Kruk R, *et al*. High-entropy oxides: An emerging prospect for magnetic rare-earth transition metal perovskites. *Phys Rev Mater* 2019, **3**: 034406.

[31] Elsiddig ZA, Xu H, Wang D, *et al*. Modulating Mn^{4+} ions and oxygen vacancies in nonstoichiometric $LaMnO_3$ perovskite by a facile sol–gel method as high-performance supercapacitor electrodes. *Electrochim Acta* 2017, **253**: 422–429.

[32] Han XY, Cui YP, Liu HW. Ce-doped Mn_3O_4 as high-performance anode material for lithium ion batteries. *J Alloys Compd* 2020, **814**: 152348.

[33] Wang M, Chen L, Liu M, *et al*. Enhanced electrochemical performance of La-doped Li-rich layered cathode material. *J Alloys Compd* 2020, **848**: 156620.

[34] Patra J, Nguyen TX, Tsai CC, *et al*. Effects of elemental modulation on phase purity and electrochemical properties of Co-free high-entropy spinel oxide anodes for lithium-ion batteries. *Adv Funct Mater* 2022, **32**: 2110992.

[35] Li S, Peng ZJ, Fu XL. $Zn_{0.5}Co_{0.5}Mn_{0.5}Fe_{0.5}Al_{0.5}Mg_{0.5}O_4$ high-entropy oxide with high capacity and ultra-long life for Li-ion battery anodes. *J Adv Ceram* 2023, **12**: 59–71.

[36] Li W, Liu J, Zhao DY. Mesoporous materials for energy conversion and storage devices. *Nat Rev Mater* 2016, **1**: 16023.

[37] Ashok A, Kumar A, Bhosale RR, *et al*. Combustion synthesis of bifunctional $LaMO_3$ (M = Cr, Mn, Fe, Co, Ni) perovskites for oxygen reduction and oxygen evolution reaction in alkaline media. *J Electroanal Chem* 2018, **809**: 22–30.

[38] Khort A, Podbolotov K, Serrano-García R, *et al*. One-step solution combustion synthesis of cobalt nanopowder in air atmosphere: The fuel effect. *Inorg Chem* 2018, **57**: 1464–1473.

[39] Biesinger MC, Payne BP, Grosvenor AP, *et al*. Resolving surface chemical states in XPS analysis of first row transition metals, oxides and hydroxides: Cr, Mn, Fe, Co and Ni. *Appl Surf Sci* 2011, **257**: 2717–2730.

[40] Guo M, Liu YF, Zhang FN, *et al*. Inactive Al^{3+}-doped $La(CoCrFeMnNiAl_x)_{1/(5+x)}O_3$ high-entropy perovskite oxides as high performance supercapacitor electrodes. *J Adv Ceram* 2022, **11**: 742–753.

[41] Sanchez JS, Pendashteh A, Palma J, *et al*. Porous NiCoMn ternary metal oxide/graphene nanocomposites for high performance hybrid energy storage devices. *Electrochim Acta* 2018, **279**: 44–56.

[42] Zhu YM, Zhang L, Zhao BT, *et al*. Improving the activity for oxygen evolution reaction by tailoring oxygen defects in double perovskite oxides. *Adv Funct Mater* 2019, **29**: 1901783.

[43] Zhang YY, Chen P, Wang QY, *et al*. High-capacity and kinetically accelerated lithium storage in MoO_3 enabled by oxygen vacancies and heterostructure. *Adv Energy Mater* 2021, **11**: 2101712.

[44] Wang DR, Li HY, Li CJ, *et al*. Oxygen-deficient and orderly mesoporous cobalt oxide nanospheres for superior lithium storage. *J Alloys Compd* 2021, **887**: 161339.

[45] Cui Y, Xiao KF, Bedford NM, *et al*. Refilling nitrogen to oxygen vacancies in ultrafine tungsten oxide clusters for superior lithium storage. *Adv Energy Mater* 2019, **9**: 1902148.

[46] Kim HS, Cook JB, Lin H, *et al*. Oxygen vacancies enhance pseudocapacitive charge storage properties of MoO_{3-x}. *Nat Mater* 2017, **16**: 454–460.

[47] Cai YX, Ku L, Wang LS, *et al*. Engineering oxygen vacancies in hierarchically Li-rich layered oxide porous microspheres for high-rate lithium ion battery cathode. *Sci China Mater* 2019, **62**: 1374–1384.

[48] Jia DD, Chen XQ, Tan H, *et al*. Boosting electrochemistry of manganese oxide nanosheets by Ostwald ripening during reduction for fiber electrochemical energy storage device. *ACS Appl Mater Interfaces* 2018, **10**: 30388–30399.

[49] Tang ZK, Xue YF, Teobaldi G, *et al*. The oxygen vacancy in Li-ion battery cathode materials. *Nanoscale Horiz* 2020, **5**: 1453–1466.

[50] Zhang N, Liu EQ, Chen HW, *et al*. High-performance of $LaCoO_3/Co_3O_4$ nanocrystal as anode for lithium-ion batteries. *Colloid Surface A* 2021, **628**: 127265.

[51] Wang SY, Chen TY, Kuo CH, *et al*. Operando synchrotron transmission X-ray microscopy study on (Mg,Co,Ni,Cu,Zn)O high-entropy oxide anodes for lithium-ion batteries. *Mater Chem Phys* 2021, **274**: 125105.

[52] Cao KZ, Jin T, Yang L, *et al*. Recent progress in conversion reaction metal oxide anodes for Li-ion batteries. *Mater Chem Front* 2017, **1**: 2213–2242.

[53] Zhang QY, Zhang CL, Li B, *et al*. Preparation and electrochemical properties of Ca-doped $Li_4Ti_5O_{12}$ as anode materials in lithium-ion battery. *Electrochim Acta* 2013, **98**: 146–152.

[54] Sarkar A, Wang QS, Schiele A, *et al*. High-entropy oxides: Fundamental aspects and electrochemical properties. *Adv Mater* 2019, **31**: 1806236.

[55] Kong YZ, Yang ZR. Synthesis, structure and electrochemical properties of Al doped high entropy perovskite $Li_x(LiLaCaSrBa)Ti_{1-x}Al_xO_3$. *Ceram Int* 2022, **48**: 5035–5039.

[56] Jia YG, Shao X, Chen J, *et al*. Preparation and lithium storage performance of pseudocapacitance-controlled chalcogenide high-entropy oxide La(Co$_{0.2}$Cr$_{0.2}$Fe$_{0.2}$Mn$_{0.2}$Ni$_{0.2}$)O$_3$ anode materials. *Chem J Chinese Universities* 2022, **43**: 20220157. (in Chinese)

[57] Ogunniran KO, Murugadoss G, Thangamuthu R, *et al*. Evaluation of nanostructured Nd$_{0.7}$Co$_{0.3}$FeO$_3$ perovskite obtained via hydrothermal method as anode material for Li-ion battery. *Mater Chem Phys* 2020, **248**: 122944.

[58] Chang LM, Li JH, Le ZY, *et al*. Perovskite-type CaMnO$_3$ anode material for highly efficient and stable lithium ion storage. *J Colloid Interf Sci* 2021, **584**: 698–705.

[59] Wang K, Hua WB, Huang XH, *et al*. Synergy of cations in high entropy oxide lithium ion battery anode. *Nat Commun* 2023, **14**: 1487.

[60] Lu CH, Lin SW. Influence of the particle size on the electrochemical properties of lithium manganese oxide. *J Power Sources* 2001, **97–98**: 458–460.

[61] Maleski K, Ren CE, Zhao MQ, *et al*. Size-dependent physical and electrochemical properties of two-dimensional MXene flakes. *ACS Appl Mater Interfaces* 2018, **10**: 24491–24498.

[62] Ghigna P, Airoldi L, Fracchia M, *et al*. Lithiation mechanism in high-entropy oxides as anode materials for Li-ion batteries: An operando XAS study. *ACS Appl Mater Interfaces* 2020, **12**: 50344–50354.

[63] Zhong Y, Xia XH, Shi F, *et al*. Transition metal carbides and nitrides in energy storage and conversion. *Adv Sci* 2016, **3**: 1500286.